Research Square

Preprints are preliminary reports that have not undergone peer review.
They should not be considered conclusive, used to inform clinical practice,
or referenced by the media as validated information.

Acute lethality and stress-responsive phenotypes differ among three Acinetobacter baumannii strains: phenotypic, genomic and transcriptomic analyses

Yue Zhu
Zhejiang University School of Medicine
Hongyan Yu
The First Affiliated Hospital of Wenzhou Medical University
Hua Zhou
hua__zhou@163.com

The Second Affiliated Hospital of Zhejiang University School of Medicine

Research Article

Keywords: Acinetobacter baumannii, acute lethality, antimicrobial resistance, biofilm, epithelial-cell association, iron acquisition, colistin, serum, transcriptomics

Posted Date: October 30th, 2026

DOI: https://doi.org/10.21203/rs.3.rs-11260125/v1

License: This work is licensed under a Creative Commons Attribution 4.0 International License.
Read Full License

Additional Declarations:
No competing interests reported.

Table 1 is available in the Supplementary Files section.

Title

Acute lethality and stress-responsive phenotypes differ among three *Acinetobacter baumannii* strains: phenotypic, genomic and transcriptomic analyses

Running title:Divergent pathogenic phenotypes of *A. baumannii*

Yue Zhu[1†],Hongyan Yu[2†],Hua Zhou[3*]

[1]Department of Critical Care Medicine, The First Affiliated Hospital, Zhejiang University School of Medicine, Hangzhou 310003, China

[2]Department of Respiratory Medicine, The First Affiliated Hospital of Wenzhou Medical University, Wenzhou 325000, China

[3]Department of Respiratory and Critical Care Medicine, The Second Affiliated Hospital of Zhejiang University School of Medicine, Hangzhou 310009, China

[†]These authors contributed equally to this work.

***Corresponding Author**: Hua Zhou
E-mail:hua__zhou@163.com

Abstract

Background

Acinetobacter baumannii exhibits substantial strain-level heterogeneity in antimicrobial resistance, virulence-associated phenotypes and responses to environmental stress. Whether acute lethality covaries with surface-associated and stress-responsive phenotypes across different strain backgrounds remains unclear. We compared three clinically distinct *A. baumannii* strains, LS01, AB5075 and XH386, using phenotypic assays, comparative genome annotation and transcriptomic profiling.

Results

The three strains displayed distinct phenotypic profiles. Following inoculation with 5 × 10^4 CFU in *Galleria mellonella*, 96-h survival was 20% for LS01, 45% for AB5075 and 60% for XH386. In immunocompetent C57BL/6J mice challenged by oropharyngeal aspiration with a common inoculum of 5 × 10^6 CFU, 120-h survival was 25% after LS01 infection, whereas all AB5075- and XH386-infected mice survived. XH386 yielded the highest HBE-cell-associated bacterial recovery in both independent experiments. OD600 trajectories during exposure to non-heat-inactivated human serum varied with serum concentration and donor; at 10% serum, XH386 showed a higher late-phase OD600 than LS01 in both donor experiments. Transmission electron microscopy showed the most prominent capsule-associated extracellular layer in AB5075, whereas LS01 showed a thinner layer and XH386 markedly attenuated capsule-associated material. Attached biomass varied with strain and environmental condition, with XH386 showing the highest biomass under 10% heat-inactivated serum in repeated experiments. Comparative genome annotation showed extensive overlap in major pathogenicity-, biofilm-, iron-acquisition-, secretion- and stress-associated systems despite these phenotypic differences. In XH386, DIP-mediated iron restriction produced the largest transcriptional response, with 1,059 genes meeting adjusted $P < 0.05$ and $|\log2 \text{ fold change}| \geq 1$. Iron-acquisition-associated loci were strongly induced by iron restriction and more modestly by heat-inactivated serum, whereas sub-inhibitory colistin was associated with coordinated repression of ribosomal, respiratory and metabolic genes.

Conclusions

LS01, AB5075 and XH386 showed no common ordering across acute lethality, surface-associated phenotypes and environmental stress responses. At the common murine challenge dose, LS01 showed the greatest acute lethality, whereas XH386 yielded the highest HBE-cell-associated bacterial recovery and repeatedly showed the highest attached biomass under 10% heat-inactivated serum. Major pathogenicity- and stress-associated functional systems were broadly shared among the three genomes, while XH386 exhibited marked condition-dependent transcriptional remodeling. Together, these findings indicate that the experimentally measured phenotypic differences among the three strains were not attributable to broad pathway presence or absence alone.

Keywords: *Acinetobacter baumannii*; acute lethality; antimicrobial resistance; biofilm; epithelial-cell association; iron acquisition; colistin; serum; transcriptomics

Background

Acinetobacter baumannii is an opportunistic Gram-negative pathogen associated with ventilator-associated and hospital-acquired pneumonia, bloodstream infection, wound infection and device-associated infection. Its clinical importance has increased with the global dissemination of multidrug-resistant lineages. Carbapenem-resistant A. baumannii (CRAB) remains classified by the World Health Organization as a critical-priority bacterial pathogen because of its substantial disease burden and limited therapeutic options [1]. The pathogenic potential of A. baumannii is multifactorial and reflects the combined contributions of surface structures, envelope composition, nutrient acquisition, stress adaptation and interactions with host cells [2].

Marked phenotypic heterogeneity has been documented among clinical A. baumannii isolates. Strains may differ in antimicrobial susceptibility, growth characteristics, motility, capsule production, biofilm formation and lethality in experimental infection models, including isolates from related clonal backgrounds [3,4]. Serum-associated phenotypes and biofilm formation also vary substantially among strains and do not necessarily covary [5]. Capsule is an important determinant of host interaction and experimental virulence, but its biological effects depend not only on capsule abundance but also on carbohydrate structure and regulatory context [6–10]. These observations indicate that individual surface-associated traits cannot be assumed to predict overall pathogenic behavior across strain backgrounds.

Interactions with host surfaces represent another important source of strain-level variation. OmpA- and fibronectin-mediated mechanisms have been implicated in the association of A. baumannii with respiratory epithelial cells [11,12]. Csu pili and poly-β-1,6-N-acetylglucosamine produced by the *pgaABCD* locus contribute to surface attachment and biofilm development [13,14], and Csu-pilus expression has also been linked to epithelial-cell adherence in some strain backgrounds [15]. The phenotypic contribution of these systems, however, is influenced by strain-specific genetic and regulatory context as well as by the surrounding environment.

Iron availability imposes a further constraint during infection. Host-mediated iron sequestration restricts extracellular iron and requires A. baumannii to rely on high-affinity acquisition systems, including siderophore-mediated uptake and ferrous-iron transport [16]. Acinetobactin, baumannoferrin and fimsbactin systems have been described in different strain backgrounds [16,17]. Disruption of acinetobactin-associated functions impairs iron acquisition and experimental virulence [18], while transcriptomic studies have demonstrated induction of siderophore-biosynthesis and iron-uptake genes under host-associated or iron-limited conditions [19]. Thus, the genomic presence of an iron-acquisition system does not necessarily predict the magnitude of its transcriptional activation under a particular environmental condition.

Antimicrobial exposure may likewise induce physiological responses beyond canonical resistance mechanisms. Colistin disrupts the Gram-negative outer membrane, and reduced susceptibility may

involve loss or modification of lipooligosaccharide, including phosphoethanolamine modification of lipid A mediated by PmrC/EptA-family enzymes [20–22]. Exposure to sub-inhibitory polymyxin concentrations can also alter biofilm-associated phenotypes [23]. Resistance-associated gene content and stress-induced transcription therefore represent related but distinct dimensions of bacterial adaptation.

Comparative genomic studies have shown that many pathogenicity-associated genes are broadly conserved within major A. baumannii lineages despite substantial heterogeneity in experimentally measured phenotypes [24,25]. This mismatch suggests that broad gene repertoire alone may be insufficient to explain differences in acute lethality, host-cell association, biofilm-associated biomass and responses to environmental stress. Integrating phenotypic measurements with genome annotation and condition-dependent transcription may therefore provide a more informative framework for examining strain-level heterogeneity.

To address this question, we compared three A. baumannii strains with distinct clinical and antimicrobial-resistance backgrounds. LS01 is a previously characterized, broadly antimicrobial-susceptible isolate recovered from the blood of a patient with severe community-acquired pneumonia [26]. AB5075 is a multidrug-resistant clinical isolate widely used as a highly virulent experimental reference strain [27]. XH386 is an ST208 multidrug-resistant clinical isolate recovered from a pediatric patient with acute bronchopneumonia and has a previously published complete genome [28]. We compared the three strains with respect to growth, antimicrobial susceptibility, acute lethality in *Galleria mellonella* and murine pulmonary infection models, capsule-associated morphology, growth-associated OD600 trajectories during exposure to non-heat-inactivated human serum, HBE-cell-associated bacterial recovery, biofilm-associated biomass and responses to altered iron availability and sub-inhibitory colistin. Uniform draft-genome annotation was used for direct three-strain genomic comparison, and XH386 was further profiled by RNA sequencing under heat-inactivated serum exposure, sub-inhibitory colistin exposure, combined serum–colistin exposure and iron restriction.

Methods

Study design

This study compared three *Acinetobacter baumannii* strains, LS01, AB5075 and XH386, using phenotypic assays and a uniform draft-genome annotation workflow. XH386 was additionally examined by RNA sequencing under heat-inactivated serum exposure, sub-inhibitory colistin exposure, combined serum–colistin exposure and iron restriction.

Bacterial strains and culture conditions

LS01 is a previously characterized, broadly antimicrobial-susceptible clinical isolate recovered from the blood of a previously healthy 52-year-old patient with severe community-acquired pneumonia in Zhejiang Province, China [26].

AB5075-UW, hereafter referred to as AB5075, is a multidrug-resistant clinical isolate recovered in 2008 from a patient with tibial osteomyelitis and subsequently established as a reference strain for studies of *A. baumannii* pathogenesis and antimicrobial treatment [27]. Its reference chromosome is available under GenBank accession number CP008706.1.

XH386 is an ST208 multidrug-resistant clinical isolate recovered in 2014 from a pediatric patient with acute bronchopneumonia in Hangzhou, China [28]. Its previously published complete genome comprises a 4,087,343-bp chromosome and a 112,157-bp plasmid, deposited under GenBank accession numbers CP010779.1 and CP010780.1, respectively (BioProject PRJNA273343).

Unless otherwise stated, bacteria were cultured in Luria–Bertani (LB) broth or on LB agar at 37 °C. Single colonies were inoculated into LB broth and cultured overnight before subculture into fresh medium and growth to logarithmic phase for subsequent experiments.

Antimicrobial susceptibility testing

Minimum inhibitory concentrations (MICs), except for colistin, were determined using the VITEK 2 Compact automated identification and antimicrobial susceptibility testing system (bioMérieux, France) with AST-GN335 cards. The antimicrobial panel included ceftazidime, cefepime, meropenem, amikacin, ciprofloxacin, tigecycline, tobramycin, imipenem, ampicillin–sulbactam, piperacillin–tazobactam, cefoperazone–sulbactam and trimethoprim–sulfamethoxazole. Where applicable, MICs were interpreted according to the Clinical and Laboratory Standards Institute (CLSI) M100, 36th edition (2026) [29].

Colistin MICs were determined separately by broth microdilution. Measured colistin MICs were used directly to define strain-specific sub-inhibitory concentrations in subsequent experiments.

Because no CLSI or US Food and Drug Administration species-specific tigecycline susceptibility breakpoints are established for *A. baumannii*, tigecycline results were reported as quantitative MIC values without assignment to susceptible, intermediate or resistant categories.

Growth kinetics

Overnight bacterial cultures were adjusted to equivalent starting optical densities and inoculated into fresh LB broth. Growth was monitored at 37 °C using a TriStar3 multi-mode microplate reader (Berthold Technologies, Germany), with OD600 recorded at approximately 5-min intervals for 20 h. LS01, AB5075 and XH386 were measured simultaneously on the same plate, with 12 technical wells per strain and three medium-only control wells. At each time point, the mean OD600 of the medium-only wells was subtracted from the corresponding bacterial measurements.

The direct experiment in which all three strains were examined simultaneously represented one independent biological experiment. Growth kinetics were therefore interpreted descriptively, and technical wells were not treated as independent biological replicates for inferential statistical testing.

Galleria mellonella infection

Medium-sized *G. mellonella* larvae were obtained from Ruiqingbait (China). Healthy larvae without visible melanization or other external abnormalities were selected for infection. Logarithmic-phase bacterial cultures were washed and resuspended in sterile PBS. Each larva was inoculated with 5 × 10^4 CFU in a 10-μL volume through the last left proleg. Twenty larvae were included in each LS01, AB5075 and XH386 group, and 20 PBS-injected larvae served as controls.

Following inoculation, larvae were maintained at 37 °C and assessed at 12-h intervals for 96 h. Larvae that failed to respond to physical stimulation were considered dead.

Growth during exposure to non-heat-inactivated human serum

De-identified residual serum specimens obtained from individuals undergoing routine health examinations were used without heat inactivation. Two independent experiments were performed using serum from different donors.

Logarithmic-phase bacterial cultures were washed and resuspended in sterile PBS before exposure to LB containing 0%, 5%, 10% or 20% human serum. Each condition was tested in technical triplicate in sterile flat-bottom 96-well plates at a final volume of 200 μL per well. Plates were incubated at 37 °C, and OD600 was measured serially for up to 24 h. Technical replicate wells were averaged within each donor experiment before interpretation.

Concentration-matched cell-free serum wells were not included for optical-density background subtraction. OD600 trajectories were therefore interpreted primarily through within-concentration, within-donor comparisons among strains. This assay was not used as a direct measure of serum bactericidal activity or complement-mediated survival.

The use of de-identified residual human serum specimens was approved by the Clinical Research Ethics Committee of the First Affiliated Hospital, Zhejiang University School of Medicine (IIT Ethics Approval No. 0198; protocol no. IIT20240878B-R1). All experiments involving these human-derived specimens were conducted in accordance with the Declaration of Helsinki and relevant institutional and national guidelines and regulations. The requirement for individual informed consent was waived by the ethics committee because only de-identified residual clinical specimens were used.

Acute murine pulmonary infection

Specific-pathogen-free female C57BL/6J mice aged 6–8 weeks were obtained from Hangzhou Qizhen Laboratory Animal Technology Co., Ltd. (Hangzhou, China). Mice were acclimated for 3 days before experimentation and housed in individually ventilated cages at 20–26 °C and 30–70% relative humidity under a 12-h light/12-h dark cycle, with food and water available *ad libitum*. Animals were randomly allocated to experimental groups before bacterial challenge. Group sizes were selected on the basis of prior experience with this murine pulmonary infection model.

Logarithmic-phase bacterial cultures were washed and resuspended in sterile PBS. Before pulmonary challenge, mice were anesthetized by intraperitoneal administration of 2,2,2-tribromoethanol (Avertin; MA0478; 1.25% solution) at 250 mg/kg, with the injection volume adjusted according to body weight. Each mouse was challenged by oropharyngeal aspiration with 5 × 10^6 CFU of LS01, AB5075, or XH386 in a final volume of 50 μL. PBS-treated animals served as controls. Briefly, anesthetized mice were suspended by the upper incisors, the tongue was gently extended, and the nares were transiently occluded. The bacterial suspension was deposited into the oropharynx and allowed to enter the respiratory tract by reflex aspiration.

For the primary equal-dose survival experiment, 20 mice were included in each bacterial group and followed for 120 h. Clinical status and survival were assessed at 12-h intervals by animal-facility personnel blinded to bacterial-strain assignment. Prespecified humane endpoints included marked hypothermia, loss of >20% of baseline body weight, severe hunching, and markedly reduced spontaneous activity. Animals reaching a humane endpoint were euthanized immediately. Mice were first deeply anesthetized by intraperitoneal administration of 2,2,2-tribromoethanol (Avertin; 1.25% solution, 250 mg/kg), with the injection volume adjusted according to body weight. Cervical dislocation was performed only after deep anesthesia had been achieved, ensuring that the animals were unconscious during the procedure. This two-step euthanasia procedure was used to minimize pain and distress and to ensure rapid and irreversible death. The time at which the humane endpoint was reached was recorded as the survival-event time.

All murine procedures were reviewed and approved by the Zhejiang University Laboratory Animal Welfare and Ethics Review Committee (approval no. ZJU20250683) and were conducted in accordance with institutional and applicable national requirements for the care and use of laboratory animals.

Exploratory dose-ranging analysis

An exploratory dose-ranging analysis incorporated the LS01 cohort challenged with 5 × 10^6 CFU (n = 20) from the primary survival experiment together with additional cohorts challenged with XH386 at 5 × 10^6 CFU (n = 10) or AB5075 at 5 × 10^7 CFU (n = 10). Ten PBS-treated mice served as controls. Survival was summarized through 120 h.

Because the LS01 cohort was shared with the primary survival experiment and the additional exploratory cohorts differed in bacterial inoculum and group size, this analysis was interpreted descriptively and was not used for direct between-strain statistical inference.

Pulmonary histopathology and scoring

Pulmonary histopathology was evaluated in separate terminal cohorts that were independent of the animals used in the primary and exploratory survival experiments. A common day-0 baseline cohort of three uninfected mice was included to document baseline pulmonary histology. Before bacterial challenge, mice assigned to the histopathology cohorts were randomly allocated to

scheduled terminal tissue collection on days 1–5, with three mice per experimental group at each time point. Animals assigned to the histopathology cohorts were not included in survival analyses.

For all scheduled terminal collections, mice were deeply anesthetized by intraperitoneal administration of 2,2,2-tribromoethanol (Avertin; 1.25% solution, 250 mg/kg), with the injection volume adjusted according to body weight. Cervical dislocation was performed only after deep anesthesia had been achieved, ensuring that the animals were unconscious during the procedure. Lung tissues were collected immediately thereafter, fixed, and processed according to the pathology laboratory standard operating procedure.

Paraffin-embedded sections were stained with hematoxylin and eosin (H&E) and examined at multiple magnifications using a Nikon Eclipse Ci-L bright-field microscope (Nikon, Japan). Representative low- and high-magnification fields were recorded.

Five pulmonary lesion domains were evaluated for each animal: alveolar-wall thickening, inflammatory-cell infiltration, bronchial epithelial-cell injury/necrosis, vascular congestion, and hemorrhage. Each lesion domain was graded independently on a 0–4 severity scale: 0, within normal limits; 1, minimal; 2, mild; 3, moderate; and 4, severe. The total pulmonary histopathology score for each animal was calculated as the sum of the five domain scores, yielding a possible range of 0–20. Scoring was performed by an evaluator blinded to experimental-group assignment.

Total pulmonary histopathology scores were summarized descriptively as mean ± SD for the three mice in the common day-0 baseline cohort and for the three mice examined per group at each subsequent post-challenge time point. No inferential between-group testing was performed.

Transmission electron microscopy

Logarithmic-phase bacterial cells were collected by centrifugation and fixed in commercial electron-microscopy fixative (Servicebio, G1102) at 4 °C for 2–4 h. After three washes with 0.1 M phosphate buffer (pH 7.4), bacterial pellets were embedded in 1% agarose and post-fixed with 1% osmium tetroxide in 0.1 M phosphate buffer for 2 h at room temperature in the dark. Samples were subsequently washed three times with phosphate buffer and dehydrated through a graded ethanol series (30%, 50%, 70%, 80%, 95% and 100%), followed by two changes of 100% acetone.

Dehydrated samples were infiltrated sequentially with acetone–812 epoxy resin mixtures and pure 812 resin and polymerized at 60 °C for 48 h. Ultrathin sections (60–80 nm) were prepared using a Leica UC7 ultramicrotome (Leica Microsystems) and collected on 150-mesh copper grids. Sections were stained with 2% uranyl acetate for 8 min followed by 2.6% lead citrate for 8 min and examined using a Hitachi HT7800 transmission electron microscope (Hitachi, Japan).

Capsule-associated extracellular morphology was evaluated qualitatively from representative sections. Apparent capsule thicknesses shown in representative micrographs were used only as descriptive morphological measurements. No inferential capsule-thickness analysis was performed because a predefined biological sampling and measurement framework had not been established.

HBE-cell association assay

HBE135-E6E7 human bronchial epithelial cells (cat. no. JY348; SSRCC, China), originally derived from ATCC CRL-2741, were cultured in Ham's F-12K medium supplemented with 10% heat-inactivated fetal bovine serum at 37 °C in a humidified atmosphere containing 5% CO_2.

Approximately 5 × 10^5 cells were seeded per well in 24-well plates approximately 16 h before bacterial challenge. One hour before infection, the culture medium was replaced with antibiotic-free medium containing heat-inactivated fetal bovine serum, and cells were treated with 4 μM cytochalasin D for 1 h to reduce actin-dependent bacterial internalization.

Logarithmic-phase cultures of LS01, AB5075 and XH386 were prepared in LB broth at 37 °C with shaking at approximately 175 rpm. Bacterial cells were collected by centrifugation, washed twice with sterile PBS and resuspended before infection. Bacterial concentrations were estimated from OD600 and adjusted to provide an approximate multiplicity of infection of 100, corresponding to approximately 5 × 10^7 CFU per well.

Bacterial suspensions were added to HBE monolayers and incubated for approximately 60 min at 37 °C in 5% CO_2. Following infection, each well was gently washed four times with prewarmed PBS to remove non-associated bacteria. Cells were lysed with 100 μL of 1% Triton X-100 in PBS for approximately 10 min at room temperature. Lysates were thoroughly mixed, serially diluted tenfold and plated on LB agar. Plates were incubated at 37 °C for 16–18 h before colony enumeration. Recovered bacterial counts were expressed as CFU per well.

Two independent biological experiments were performed, with three technical wells per strain in each experiment. Technical wells were summarized within each independent experiment and were not treated as independent biological replicates for inferential statistical testing.

Because complete experimentally verified inoculum counts were not available for all experiments, recovered bacterial counts were not normalized to the nominal inoculum and were not expressed as an adhesion percentage. In addition, although cytochalasin D was used to reduce actin-dependent internalization, complete exclusion of intracellular bacteria was not independently demonstrated. The assay endpoint was therefore interpreted as HBE-cell-associated bacterial recovery rather than as a quantitative measure of adhesion efficiency.

Crystal-violet biofilm assay

Attached biofilm biomass was quantified using a crystal-violet microtiter assay. Single bacterial colonies were inoculated into LB broth and cultured at 37 °C with shaking at 200 rpm for 12–16 h. Cultures were subsequently diluted into fresh medium and grown for a further 4–6 h, washed with PBS and adjusted to OD600 = 0.1.

Standardized bacterial suspensions were dispensed into sterile flat-bottom 96-well plates at a final volume of 200 μL per well and incubated statically at 37 °C for 24 h. Core experimental conditions comprised untreated baseline, 5% heat-inactivated human serum, 10% heat-inactivated

human serum, strain-specific 1/4-MIC colistin and combined 5% heat-inactivated serum plus 1/4-MIC colistin. Additional conditions, including 1/8-MIC and 1/2-MIC colistin and higher-serum combination conditions, were examined in exploratory experiments.

The heat-inactivated human serum used in these experiments was obtained from a single donor and heat-inactivated at 56 °C for 30 min. Based on the measured colistin MICs, the 1/4-MIC concentrations were 0.0625 mg/L for LS01, 0.125 mg/L for AB5075 and 0.0625 mg/L for XH386. The corresponding 1/2-MIC concentrations were 0.125, 0.25 and 0.125 mg/L, respectively.

After incubation, planktonic material was removed and wells were washed three times with 200 µL PBS. Attached material was fixed with 200 µL 100% methanol for 15 min and air dried. Wells were stained with 200 µL 0.1% crystal violet for 15–20 min, washed three to four times with PBS and air dried for at least 30 min. Bound crystal violet was solubilized with 200 µL 95% ethanol for 10–15 min, and absorbance was measured at 570 nm after subtraction of the corresponding blank-well signal.

The assays were performed across multiple independent experimental batches, although the number of independent batches differed among conditions. Each batch included technical replicate wells, which were averaged before interpretation and were not treated as independent biological replicates. Comparisons therefore focused on reproducibility of within-batch strain ordering and condition-associated changes rather than on pooling raw OD570 measurements across experimental batches. Exact experiment-level source data and replicate structure are provided in Supplementary Data S1.

Iron restriction and iron repletion

Iron availability was manipulated using 2,2′-dipyridyl (DIP) and ferric chloride ($FeCl_3$). DIP was tested at final concentrations of 100 and 200 µM. In iron-repletion experiments, $FeCl_3$ was added at final concentrations of 10, 50 or 100 µM.

Iron-chelation experiments were performed using 100 or 200 µM DIP. For the iron-repletion experiments shown in Fig. 4B–D, $FeCl_3$ was added at 10, 50 or 100 µM against a 100 µM DIP background. $FeCl_3$ repletion was evaluated within the DIP background used in the corresponding experiment. Because the iron-restriction background differed among batches, each experiment was interpreted relative to its matched untreated and DIP-only controls, and raw OD570 values were not pooled across batches. Attached biomass was quantified using the crystal-violet assay described above.

Comparative genomic analysis

For direct three-strain genomic comparisons, newly generated Illumina whole-genome sequencing data for LS01, AB5075 and XH386 were analyzed using the same short-read draft-genome workflow. Paired-end 150-bp sequencing generated 3.289 Gb of clean sequence data for LS01, 2.196 Gb for AB5075 and 2.133 Gb for XH386, with Q30 values of 98.12%, 97.85% and 97.84%, respectively.

Quality-filtered reads from each strain were assembled independently using SOAPdenovo v2.04, SPAdes and ABySS. The resulting assemblies were integrated using CISA and further optimized by gap closing with GapClose v1.12. Sequences shorter than 500 bp were excluded from the final draft-assembly statistics. Protein-coding genes were predicted using GeneMarkS v4.17.

The resulting draft assemblies comprised 3,718,166 bp in 16 scaffolds for LS01, 4,076,479 bp in 41 scaffolds for AB5075 and 4,389,141 bp in 56 scaffolds for XH386, with scaffold N50 values of 471,559, 219,066 and 149,071 bp, respectively. These uniformly generated short-read draft assemblies were used for direct cross-strain comparisons.

The previously published complete XH386 genome (CP010779.1 and CP010780.1) was used only to describe the strain background and was not substituted for the project-specific XH386 draft assembly in the direct three-strain comparison.

Genomic islands were predicted using IslandPath-DIMOB v0.2, prophage regions using PhiSpy v2.3 and CRISPR arrays using CRISPRdigger v1.0. Gene Ontology and KEGG annotations were used to describe broad functional distributions. KEGG Orthology assignments were compared across strains and interpreted as annotation overlap rather than as a formal core-genome or pangenome analysis.

Virulence-associated proteins were annotated against the Virulence Factor Database using DIAMOND. Pathogen–host interaction-associated homologues were annotated against PHI-base, and antimicrobial-resistance-associated genes were annotated against the Comprehensive Antibiotic Resistance Database using the Resistance Gene Identifier pipeline [30]. These database-derived results were interpreted as homology-based functional annotations rather than as direct quantitative measures of virulence or pathogenic potential.

Comparative analyses focused on resistance determinants and selected systems relevant to the experimentally examined phenotypes, including capsule- and surface-associated functions, biofilm loci, iron-acquisition systems, secretion systems and stress-response regulators.

RNA sequencing of XH386 under environmental stress

XH386 was examined under five experimental conditions: untreated control, 10% (v/v) heat-inactivated human serum, 1/2-MIC colistin, combined 10% heat-inactivated human serum plus 1/2-MIC colistin, and 100 μM DIP. Each condition comprised three independent biological replicates. The human serum used for transcriptomic profiling was obtained from a single donor and heat-inactivated at 56 °C for 30 min before use. The colistin MIC of XH386 was 0.25 mg/L; the 1/2-MIC concentration used for transcriptomic profiling was therefore 0.125 mg/L.

Each biological replicate was initiated independently from a separate single bacterial colony. Individual colonies were inoculated into separate LB cultures and incubated overnight at 37 °C with shaking at 180 rpm for 16–18 h. Each independently established overnight culture was subsequently transferred to fresh LB containing the designated treatment and cultured independently at 37 °C with shaking at 180 rpm until logarithmic phase, defined as an OD600 of

approximately 0.4–0.6. This second culture typically required 4–6 h, and the designated treatment was present throughout this period.

Cells from each biological replicate were harvested independently by centrifugation at 5,000 × *g* for 5 min at 4 °C. Supernatants were removed, and bacterial pellets were immediately frozen in liquid nitrogen before RNA extraction.

Total RNA was extracted and subjected to quality assessment before library construction. Ribosomal RNA was depleted from total RNA, and the remaining RNA was fragmented. Strand-specific libraries were constructed using random-hexamer-primed first-strand cDNA synthesis followed by dUTP-based second-strand synthesis. Libraries subsequently underwent end repair, A-tailing, adaptor ligation, size selection, amplification and purification. Library concentration was assessed by Qubit fluorometry and quantitative PCR, and fragment-size distribution was assessed using an Agilent 2100 Bioanalyzer. Qualified libraries were pooled and subjected to paired-end Illumina sequencing.

Raw reads were filtered using fastp [31]. Read pairs were removed when adaptor sequences were detected, when either read contained >10% ambiguous bases, or when >50% of bases in either read had Phred quality scores ≤5. Q20, Q30 and GC content were calculated for the resulting clean reads, and all downstream analyses were performed using the clean-read dataset.

Clean reads were aligned to the project-specific XH386 draft genome assembly used in the three-strain genomic analysis using Bowtie2 v2.5.4 [32]. Gene-level read counts were generated using featureCounts v2.1.1 [33]. Reads with mapping quality <10, non-paired alignments and reads mapping to multiple genomic regions were excluded from gene-level quantification.

Differential expression was analyzed from raw read counts using DESeq2 v1.42.0 [34]. *P* values were adjusted for multiple testing using the Benjamini–Hochberg method. Genes with adjusted $P < 0.05$ were considered statistically significant; analyses emphasizing transcriptional effect size additionally applied $|\log2 \text{ fold change}| \geq 1$. FPKM values were used for sample-correlation and principal-component analyses. GO and KEGG enrichment analyses were performed using clusterProfiler v4.8.1 [35].

Prespecified pairwise contrasts were 10% heat-inactivated serum versus control, colistin versus control, combined serum–colistin versus control, DIP versus control, combined serum–colistin versus serum alone, and combined serum–colistin versus colistin alone. No formal serum-by-colistin interaction term was included; combined-treatment results were therefore interpreted from pairwise contrasts and were not used to infer statistical interaction, synergy or antagonism.

Statistical analysis

The individual larva or mouse was considered the experimental unit for survival analyses. Survival distributions were estimated using the Kaplan–Meier method and compared using the log-rank test. In the murine survival experiments, animals euthanized after reaching prespecified

humane endpoints were treated as deaths at the corresponding observation time. Mice assigned to the separate terminal histopathology cohorts were excluded from all survival analyses. Where pairwise survival comparisons were performed, *P* values were adjusted using the Holm method. The exploratory murine dose-ranging analysis was summarized descriptively and was not used for inferential between-strain comparisons because the LS01 cohort was shared with the primary survival experiment and the additional cohorts differed in inoculum and group size.

For in vitro assays, technical replicate wells were summarized within each independent biological experiment or experimental batch and were not treated as independent observations. The direct three-strain growth experiment containing AB5075 represented one independent biological experiment and was therefore interpreted descriptively. The experiments using non-heat-inactivated human serum comprised two independent donor experiments and were likewise interpreted descriptively at the donor-experiment level.

Pulmonary histopathology was assessed in terminal cohorts independent of the survival experiments. For each mouse, the total pulmonary histopathology score was calculated as the sum of the five lesion-domain scores, yielding a possible range of 0–20. Scores were summarized as mean ± SD for the common day-0 uninfected cohort and for each experimental group at subsequent post-challenge time points. Because three mice were examined per group at each time point, histopathology data were interpreted descriptively and no inferential between-group testing was performed.

HBE-cell-associated bacterial recovery was assessed in two independent biological experiments, each containing three technical wells per strain. Technical replicate wells were summarized within each experiment, and geometric mean recovered CFU was used for descriptive presentation. Because absolute bacterial recovery differed substantially between the two independent experiments, measurements were not pooled across experiments and no inferential between-strain testing was performed. Interpretation focused on the reproducibility of relative strain ordering across the two experiments.

For biofilm assays, technical replicate wells were averaged within each experimental batch and were not treated as independent biological replicates. Conditions examined in more than one independent batch were interpreted according to the reproducibility of within-batch strain and treatment patterns, whereas conditions examined in a single exploratory batch were summarized descriptively. Iron-manipulation experiments were interpreted relative to their corresponding untreated and DIP-only controls within each experimental batch because the DIP concentration differed among experiments. Raw OD570 values were not pooled across batches with different experimental conditions.

For RNA-seq analyses, differential gene expression was assessed from raw read counts using DESeq2. Multiple-testing correction was performed using the Benjamini–Hochberg procedure. Genes with an adjusted $P < 0.05$ were considered statistically significant; analyses emphasizing transcriptional effect size additionally applied an absolute log2 fold-change threshold of ≥1. Principal-component and sample-correlation analyses were based on FPKM values. No formal serum-by-colistin interaction term was fitted; therefore, comparisons involving the combined

serum–colistin condition were interpreted from prespecified pairwise contrasts and were not used to infer statistical interaction, synergy or antagonism.

Statistical analyses were performed using GraphPad Prism version 10 and R version 4.5.0. All statistical tests were two-sided where applicable.

Results

LS01, AB5075 and XH386 show distinct growth and antimicrobial-susceptibility profiles

The three strains showed different growth trajectories when examined simultaneously under the same culture conditions. After subtraction of the mean signal from the medium-only control wells, the mean OD600 values at 20 h were 1.300 for LS01, 1.253 for XH386 and 1.169 for AB5075. LS01 and XH386 showed an earlier rise in OD600 than AB5075 in this experiment. Because the direct three-strain comparison containing AB5075 was performed as a single independent biological experiment, these growth data were interpreted descriptively and were not subjected to inferential between-strain testing (Fig. 1A).

Antimicrobial-susceptibility profiles differed substantially among the three strains. Meropenem and imipenem MICs were both 0.25 mg/L for LS01, compared with 64 and 32 mg/L, respectively, for AB5075 and ≥16 mg/L for both agents for XH386. Colistin MICs were 0.25 mg/L for LS01, 0.50 mg/L for AB5075 and 0.25 mg/L for XH386. Selected MICs are shown in Fig. 1B; complete MIC profiles are provided in Supplementary Table S1.

LS01 shows greater acute lethality at the common challenge dose

Following inoculation with 5 × 10^4 CFU per larva, survival of *Galleria mellonella* declined most rapidly in the LS01 group. At 96 h, 4 of 20 larvae remained alive in the LS01 group, compared with 9 of 20 in the AB5075 group and 12 of 20 in the XH386 group. All PBS-injected larvae survived (Fig. 1C).

Overall survival differed among the three bacterial groups (log-rank $P = 0.0177$). After Holm adjustment for pairwise comparisons, survival differed between LS01 and XH386 (adjusted $P = 0.0090$), whereas the LS01-versus-AB5075 and AB5075-versus-XH386 comparisons were not statistically significant.

A more pronounced separation was observed in the primary equal-dose murine pulmonary infection experiment. Following oropharyngeal aspiration of 5 × 10^6 CFU, survival at 120 h was 25% in the LS01 group (5/20), whereas all AB5075- and XH386-infected mice survived. Overall survival differed significantly among the three bacterial groups (log-rank $P < 0.0001$) (Fig. 1D). Animals euthanized after reaching prespecified humane endpoints were treated as deaths at the corresponding observation time for survival analysis.

Pulmonary histopathology was evaluated in separate terminal cohorts independent of the animals used for survival analysis. A common cohort of three uninfected mice was examined at day 0 to

establish the pre-challenge pulmonary histologic baseline, and three mice per experimental group were examined at each subsequent prespecified post-challenge time point. Mean total pulmonary histopathology scores, calculated as the sum of five lesion-domain scores and ranging from 0 to 20, were highest in the LS01 group from day 2 through day 5. Scores in the AB5075 and XH386 groups declined toward day 5 and remained low in PBS-treated animals. Representative day-3 H&E sections and longitudinal total pulmonary histopathology scores are shown in Fig. 1E,F. These data were summarized descriptively, and no inferential between-group testing was performed.

The exploratory dose-ranging analysis incorporated the same LS01 cohort from the primary survival experiment. At 120 h, survival in this LS01 cohort was 25% (5/20). All mice in the additional XH386 cohort challenged with 5 × 10^6 CFU survived (10/10), whereas survival was 40% (4/10) in the AB5075 cohort challenged with 5 × 10^7 CFU. All PBS-treated animals survived (10/10). Because the LS01 cohort was shared with the primary experiment and the additional cohorts differed in bacterial inoculum and group size, these findings were interpreted descriptively and were not used for direct statistical comparison among strains (Supplementary Fig. S1).

OD600 trajectories during exposure to non-heat-inactivated human serum vary with concentration and donor

OD600 trajectories during exposure to non-heat-inactivated human serum varied with both serum concentration and donor. At 5% serum, the relative pattern differed markedly between the two independent donor experiments. At 10% serum, XH386 showed a higher late-phase OD600 than LS01 in both donor experiments, whereas the response of AB5075 differed between donors. At 20% serum, all three strains showed little increase in OD600 over the observation period.

Because concentration-matched cell-free serum blanks were not included, absolute OD600 values across different serum concentrations were interpreted cautiously. Between-strain comparisons within a given serum concentration and donor were made against the same serum matrix background. Representative trajectories from one donor experiment are shown in Fig. 2C–F.

Capsule-associated morphology differs among the three strains

Transmission electron microscopy revealed clear differences in capsule-associated extracellular morphology among the three strains. In representative AB5075 sections, a relatively uniform and prominent capsule-associated extracellular layer surrounded the bacterial surface. LS01 showed a thinner and less continuous layer, whereas XH386 showed markedly attenuated capsule-associated material that was absent over much of the bacterial surface, with only sparse extracellular material visible in limited regions.

Cell-wall and cytoplasmic-membrane integrity was preserved in representative sections from all three strains. Because capsule-associated morphology was assessed from representative sections without a predefined quantitative biological sampling and measurement framework, these

observations were interpreted descriptively rather than as quantitative measurements of capsule thickness (Fig. 2A,B).

XH386 yields the highest HBE-cell-associated bacterial recovery in both independent experiments

XH386 yielded the highest HBE-cell-associated bacterial recovery in both independent experiments. In the first experiment, geometric mean recovered counts were approximately 6.7 × 10^7 CFU/well for LS01, 5.7 × 10^7 CFU/well for AB5075 and 8.8 × 10^8 CFU/well for XH386. In the second experiment, the corresponding values were approximately 8.0 × 10^4, 2.2 × 10^6 and 9.2 × 10^6 CFU/well, respectively.

Absolute bacterial recovery differed substantially between the two experiments, but XH386 ranked highest in both. The relative ordering of LS01 and AB5075 differed between experiments. Because complete experimentally verified inoculum counts were not available for all experiments, recovered bacterial counts were not normalized to the nominal inoculum and were interpreted as HBE-cell-associated bacterial recovery rather than quantitative adhesion efficiency (Fig. 2G,H).

Biofilm-associated biomass varies with strain and environmental condition

Crystal-violet staining varied among independent experimental batches; comparisons were therefore made primarily within individual experiments rather than by pooling absolute OD570 values across batches. Under untreated conditions, no fixed ordering of attached biomass was observed among the three strains, although LS01 showed comparatively lower values than XH386 or AB5075 in several experiments.

Heat-inactivated human serum produced concentration- and strain-dependent changes in attached biomass. At 5% serum, the relative strain ordering varied among independent experiments. Across the independent experimental batches in which 10% heat-inactivated serum was examined, XH386 repeatedly showed the highest attached biomass, whereas AB5075 showed lower and more variable values and LS01 generally remained comparatively low.

Strain-specific 1/4-MIC colistin also altered attached biomass. XH386 and AB5075 generally showed greater crystal-violet staining than LS01 under this condition, although the relative ordering of XH386 and AB5075 varied among independent experimental batches. Combined heat-inactivated serum and sub-inhibitory colistin exposure produced additional changes in some strain–condition combinations, but neither the magnitude nor the relative strain ordering was uniform across experiments.

Additional conditions involving 1/8-MIC or 1/2-MIC colistin and higher-serum combination treatments were examined in exploratory experiments and were interpreted descriptively. Across the repeatedly examined stress conditions, the most reproducible strain-associated pattern was the comparatively high attached biomass of XH386 during exposure to 10% heat-inactivated serum (Fig. 3).

Iron availability modifies attached biomass without producing a uniform strain response

DIP-mediated iron restriction altered attached biofilm biomass in a concentration- and strain-dependent manner. At 100 μM DIP, crystal-violet staining was not consistently reduced and was maintained or increased relative to the corresponding untreated condition in several experiments. Exposure to 200 μM DIP produced more pronounced reductions in several strain–experiment combinations, although the response remained heterogeneous across strains.

In a separate iron-repletion experiment using a 100 μM DIP background, $FeCl_3$ supplementation at 10, 50 and 100 μM altered attached biomass, with increases observed in several strain–condition combinations. The magnitude and direction of the response varied among strains. These findings indicate that altered iron availability affected attached biomass but did not produce a uniform phenotypic response across the three strain backgrounds (Fig. 4).

Comparative genome annotation shows extensive overlap in major functional systems despite differences in assembly content

Uniform short-read draft-genome analysis showed differences in assembly content among the three strains. LS01 had the smallest draft assembly (3,718,166 bp), followed by AB5075 (4,076,479 bp) and XH386 (4,389,141 bp). The corresponding numbers of predicted protein-coding genes were 3,494, 3,957 and 4,224, respectively. Coding density was similar among strains, ranging from 86.67% to 87.38%.

The LS01, AB5075 and XH386 draft assemblies comprised 16, 41 and 56 scaffolds, respectively, with scaffold N50 values of 471,559, 219,066 and 149,071 bp. Predicted genomic islands, prophage regions and CRISPR arrays also differed among the assemblies and are summarized in Supplementary Table S2.

Broad GO and KEGG functional distributions were similar among strains. A total of 1,568 KEGG Orthology assignments were shared among LS01, AB5075 and XH386, accounting for more than 90% of the KO repertoire of each strain.

Systems relevant to the phenotypes examined experimentally were represented in all three genomes. These included acinetobactin-associated functions, *feoA/feoB*-associated ferrous-iron transport, TonB-dependent transport, Csu fimbriae, PNAG-associated functions, type IV pili, type II and type VI secretion systems, the *pgaABCD* biofilm locus and the stress-response regulators *rpoN*, *relA* and *spoT*. VFDB annotation also showed substantial overlap: 98 of 116 distinct VFDB factor identifiers detected across the three strains were shared by all three. When PHI-base analysis was restricted to entries annotated with *A. baumannii* as the pathogen, 49 named determinants were shared among the three strains, including *ompA, basD, tssM, relA, gigA, gigB, gspD, clpB, csrA* and *PLD1–PLD3*.

Resistance-associated annotation showed greater between-strain differentiation. LS01 contained intrinsic β-lactamase and efflux-associated determinants, including OXA-91 and ADC-2, but lacked the acquired carbapenemase repertoire present in the two multidrug-resistant strains.

AB5075 contained exact or near-exact CARD best hits to OXA-23, GES-11 and OXA-69, together with additional aminoglycoside-, trimethoprim-, sulfonamide- and efflux-associated determinants. XH386 contained exact or near-exact best hits to OXA-23, OXA-66 and TEM-1 together with *armA, tet(B), sul1* and *sul2*, among other resistance-associated determinants. Complete CARD annotations are provided in Supplementary Table S4. Representative circular genome maps and a summary of the observed phenotype combinations are shown in Fig. 5; direct cross-strain assembly-size comparisons are based on the uniformly generated short-read draft assemblies summarized in Supplementary Table S2.

RNA-seq identifies distinct stress-associated transcriptional states in XH386

RNA sequencing was performed on 15 independently established XH386 cultures representing five experimental conditions, with three biological replicates per condition. Clean sequence yield ranged from 1.05 to 1.36 Gb per sample, and Q30 values ranged from 97.11% to 98.61%. Total mapping rates were 98.21–98.64%, with 94.72–96.97% of reads mapping uniquely to the project-specific XH386 draft assembly.

Principal-component analysis separated untreated controls from stress-exposed cultures. PC1 accounted for 46.05% of total variance and PC2 for 14.29%. Biological replicates from the same condition clustered closely. DIP-treated cultures showed the greatest separation from untreated controls, whereas cultures exposed to 10% heat-inactivated serum, colistin or combined serum–colistin occupied more closely related positions in global expression space.

Using an adjusted $P < 0.05$ threshold, 1,941 genes were differentially expressed during 10% heat-inactivated serum exposure relative to control, 1,933 during colistin exposure, 2,052 during combined serum–colistin exposure and 2,067 during DIP-mediated iron restriction. Comparisons of combined treatment with serum alone and colistin alone identified 772 and 1,340 differentially expressed genes, respectively.

After application of an additional $|\log2 \text{ fold change}| \geq 1$ threshold, 842 genes met both criteria for serum versus control, 844 for colistin versus control, 944 for combined exposure versus control and 1,059 for DIP versus control. The corresponding numbers were 45 for combined treatment versus serum alone and 287 for combined treatment versus colistin alone. Among the four stress-versus-control comparisons, DIP-mediated iron restriction yielded the largest number of genes meeting both the adjusted *P*-value and fold-change thresholds (Fig. 6A,B).

Iron restriction produces the strongest induction of iron-acquisition-associated loci in XH386

A prominent iron-acquisition-associated region contained genes annotated as *dhbF*-like, *entB*-like, *entC*-like, *fatB*-like, *fatC*-like, *fatD*-like and *irtB*-like, together with additional siderophore-biosynthesis and iron-transport genes. Expression of these loci changed little during colistin exposure alone but increased during 10% heat-inactivated serum exposure and combined serum–colistin exposure. The largest increases occurred during DIP-mediated iron restriction.

Under DIP treatment, representative log2 fold changes within this region were +9.18 for *fatD*, +8.54 for *fatC*, +7.27 for *entC*, +7.25 for an *entB*-like locus and +6.82 for *dhbF*. Under 10% heat-inactivated serum exposure, the corresponding changes included +3.71 for *fatD*, +3.07 for *fatC*, +2.59 for *dhbF* and +2.40 for the same *entB*-like locus.

A second iron-associated region containing *fbsK*-, *fhuE*-, *iutA*-, *sbn*- and *rhb*-like annotations showed a similar pattern, with marked induction during DIP treatment and smaller changes during heat-inactivated serum exposure. The amplitude of induction was greater under direct chemical iron restriction than under the serum condition used in this study (Fig. 6C,D).

Sub-inhibitory colistin alters ribosomal, respiratory and envelope-associated transcription in XH386

Sub-inhibitory colistin exposure was accompanied by coordinated downregulation of multiple ribosomal genes, including *rplB, rpsS, rplV, rpsC, rplP, rplW* and *rpmC*. Among these, *rpsC* showed an approximately −3.60 log2 fold change relative to untreated control. Respiratory and metabolic genes were also affected, including *nuoF* (approximately −3.02 log2 fold) and *fadB* (approximately −2.94 log2 fold).

The transcriptional state during combined heat-inactivated serum–colistin exposure differed from that observed during colistin exposure alone and was globally closer to the profile observed during heat-inactivated serum exposure.

XH386_GM001905, annotated as an *eptA*-like phosphoethanolamine transferase, was induced under multiple environmental conditions. Relative to untreated control, its log2 fold change was approximately +4.31 during heat-inactivated serum exposure, +3.78 during colistin exposure, +4.93 during combined serum–colistin exposure and +3.37 during DIP-mediated iron restriction. A second *eptA*-annotated locus showed little corresponding change, and *pmrA* was not comparably induced. The induction pattern of XH386_GM001905 was therefore not specific to colistin exposure (Fig. 6F).

Discussion

The three *Acinetobacter baumannii* strains differed substantially across the phenotypes examined, but these differences did not follow a common strain ranking. LS01 produced the greatest acute lethality in both *Galleria mellonella* and the primary murine pulmonary infection model. XH386, by contrast, caused no mortality at the common murine challenge dose but yielded the highest HBE-cell-associated bacterial recovery in both independent experiments and repeatedly produced high attached biomass during exposure to 10% heat-inactivated human serum. AB5075 combined multidrug resistance with a prominent capsule-associated extracellular layer and intermediate lethality in *G. mellonella*. Thus, acute lethality, antimicrobial resistance and surface-associated phenotypes were not concordant across the three strain backgrounds.

The infection models provided the clearest evidence of this divergence. *Galleria mellonella* is widely used for comparative studies of *A. baumannii* pathogenicity [36], whereas murine

pulmonary infection incorporates mammalian host responses and is strongly influenced by strain background, inoculum and challenge route [37]. At a common pulmonary inoculum of 5 × 10^6 CFU, 120-h survival was 25% in the LS01 group, whereas all mice infected with AB5075 or XH386 survived. LS01 also produced the lowest 96-h survival in *G. mellonella*. In the separate terminal histopathology cohorts, pulmonary injury after LS01 challenge remained more pronounced from day 2 through day 5. Because histopathology and survival were assessed in independent animals, these outcomes were not analyzed as paired measures; nevertheless, both experiments supported a more severe acute phenotype associated with LS01 under the conditions tested.

The AB5075 findings emphasize the importance of experimental context when interpreting virulence phenotypes. AB5075 is widely used as a highly virulent reference strain [27], yet no mortality occurred at 5 × 10^6 CFU in the primary murine experiment. In the exploratory experiment, challenge with 5 × 10^7 CFU was associated with 40% survival at 120 h. This higher-dose cohort was not part of a formal dose-response design and differed from the primary experiment in both inoculum and group size. The result should therefore be regarded as evidence that the apparent lethality of AB5075 was sensitive to the challenge conditions used, rather than as proof of a quantitative dose-response relationship. Conversely, the absence of mortality at 5 × 10^6 CFU should not be taken to imply intrinsically low pathogenic potential.

Antimicrobial resistance followed a different pattern from acute lethality. LS01 was broadly susceptible to the antimicrobials tested, whereas AB5075 and XH386 were multidrug resistant and carbapenem resistant. Resistance-associated annotation was consistent with these phenotypes: AB5075 and XH386 carried acquired carbapenemases and broader accessory resistance repertoires, whereas LS01 had a more limited resistance-gene profile. With only three strains, no population-level relationship between resistance and pathogenicity can be inferred. Within this comparison, however, the strain with the greatest acute lethality did not possess the broadest resistance repertoire. Similar dissociation between antimicrobial resistance and experimentally measured pathogenicity-associated traits has been reported in larger collections of clinical *A. baumannii* isolates [3,4,25].

Capsule-associated morphology likewise did not parallel acute lethality. AB5075 showed the most prominent and continuous extracellular capsule-associated layer in representative TEM sections, LS01 showed a thinner and less continuous layer, and XH386 showed markedly attenuated capsule-associated material. Despite this ordering, LS01 was the most lethal strain at the common murine challenge dose. Capsule is an important determinant of host interaction and protection from host defenses in *A. baumannii* [6,7], but its biological effects depend on capsular composition, structure and regulation as well as apparent abundance [8]. Clinical isolates also differ considerably in complement sensitivity [9], and hypercapsulation may confer advantages under some host-associated conditions while imposing costs on other phenotypes, including attachment and growth [10]. The TEM observations in the present study therefore document clear morphological differences but do not support capsule prominence alone as a surrogate for acute lethality.

Responses to non-heat-inactivated human serum also varied by strain, serum concentration and donor. At 10% serum, XH386 showed a higher late-phase OD600 than LS01 in both donor experiments, whereas the relative pattern at 5% serum differed between donors. Concentration-matched cell-free serum controls were not included, so changes in optical background across serum concentrations could not be fully separated from changes attributable to bacterial growth. Comparisons are therefore most reliable within a given serum concentration and donor, where all strains were exposed to the same matrix background. These experiments were not designed to quantify complement-mediated killing or serum bactericidal activity. The observed variability is nevertheless consistent with previous reports of marked strain-to-strain differences in serum and complement phenotypes [5,9].

The HBE-cell association assays produced a more reproducible relative pattern. XH386 yielded the highest HBE-cell-associated bacterial recovery in both independent experiments, despite substantial differences in absolute recovered CFU between experiments. OmpA- and fibronectin-mediated mechanisms have been implicated in *A. baumannii* interactions with respiratory epithelial cells [11,12], and Csu pili may also contribute to epithelial-cell association in some strain backgrounds [15]. In the present experiments, cytochalasin D was used to reduce actin-dependent internalization, but intracellular bacteria were not quantified separately, and complete experimentally verified inoculum counts were not available for all experiments. The assay therefore cannot be interpreted as a quantitative measurement of adhesion efficiency. Its principal contribution is the reproducible observation that XH386 yielded the highest cell-associated bacterial recovery under both experimental runs.

Biofilm-associated biomass was similarly dependent on both strain and environment. Csu pili and PNAG are well-established contributors to attachment and biofilm development in *A. baumannii* [13–15], but their phenotypic effects vary across strain backgrounds and experimental conditions. Baseline crystal-violet staining did not show a stable strain hierarchy, and responses to 5% heat-inactivated serum varied among experimental batches. In contrast, XH386 repeatedly produced the highest attached biomass in experiments containing 10% heat-inactivated serum. Sub-inhibitory colistin also altered attached biomass, although the relative responses of XH386 and AB5075 were not consistent among batches. These results are compatible with previous observations that sub-MIC polymyxin exposure can modify biofilm-associated phenotypes without producing a uniform response across isolates [23].

Crystal-violet staining measures total surface-associated biomass rather than viable bacterial burden and does not distinguish bacterial cells from retained extracellular material. This limitation is particularly important when interpreting the iron-manipulation experiments. DIP-mediated iron restriction did not uniformly reduce attached biomass, and $FeCl_3$ supplementation in a 100 μM DIP background produced heterogeneous responses across strains. These experiments therefore show that altered iron availability can modify attached biomass, but they do not establish a common hierarchy of iron-starvation tolerance, viability or biofilm fitness among LS01, AB5075 and XH386.

The XH386 transcriptomic response to iron restriction was more consistent. Among the four stress-versus-control comparisons, DIP exposure produced the largest number of genes meeting

both the adjusted *P*-value and fold-change criteria. Siderophore-biosynthesis and iron-transport genes were among the most strongly induced loci, and many of the same genes were induced to a lesser extent during exposure to 10% heat-inactivated serum. Acinetobactin and other iron-acquisition systems are required for growth under iron-limited conditions and contribute to experimental pathogenicity in *A. baumannii* [16–18]. Increased expression of siderophore- and iron-uptake genes has also been reported in infection-associated transcriptomic studies [19]. The present data therefore support a strong iron-acquisition response by XH386 during experimentally imposed iron restriction, with a lower-amplitude response under the serum condition used here.

Comparative genome annotation showed substantial conservation of major functional systems despite the marked phenotypic differences among the strains. More than 90% of the KEGG Orthology repertoire of each strain was shared, and genes associated with iron acquisition, biofilm formation, secretion and stress responses were present in all three uniformly generated draft genomes. VFDB and PHI-base annotation showed a similar degree of overlap. Larger genomic studies have likewise found broad conservation of many pathogenicity-associated genes across major *A. baumannii* lineages despite considerable variation in experimentally measured phenotypes [24,25]. Homology-based annotation identifies potential functional capacity, but it does not measure pathway activity. Differences in allele sequence, genomic context, gene dosage, basal expression and regulatory responses may therefore contribute to phenotypic divergence even when the same broad functional systems are present.

This distinction is important because transcriptomic profiling in the present study was restricted to XH386. The data cannot be used to compare regulatory responses directly among LS01, AB5075 and XH386. They do, however, show that XH386 deploys substantially different transcriptional programs under iron restriction, serum exposure and sub-inhibitory colistin exposure. Regulatory networks in *A. baumannii* can coordinate antimicrobial resistance, environmental adaptation and pathogenicity-associated functions [38]. Differences in regulation therefore remain a plausible source of strain-level phenotypic variation, although direct comparative transcriptomic experiments across all three strains would be required to test this possibility.

Resistance-associated annotation showed a closer correspondence with antimicrobial-susceptibility phenotype than broad pathogenicity-associated annotation showed with acute lethality. AB5075 carried exact or near-exact CARD best hits to OXA-23, GES-11 and several additional resistance-associated determinants. XH386 carried OXA-23, OXA-66 and TEM-1 together with *armA*, *tet(B)*, *sul1* and *sul2*, among other determinants. LS01 lacked the acquired carbapenemase repertoire detected in the two multidrug-resistant strains. The contrast suggests that antimicrobial susceptibility can, in some cases, be linked relatively directly to identifiable resistance determinants, whereas complex host-interaction phenotypes are more likely to depend on combinations of structural, regulatory and environmental factors.

Sub-inhibitory colistin exposure produced broad transcriptional changes in XH386. Multiple ribosomal genes were downregulated together with genes involved in respiratory and metabolic functions, including *nuoF* and *fadB*. This pattern is compatible with a wider physiological response to membrane-active antibiotic stress rather than a response limited to canonical polymyxin-resistance pathways. The combined serum–colistin condition also differed from

colistin exposure alone and was globally closer to the serum-exposed transcriptional state. Because the analysis relied on prespecified pairwise contrasts and did not include a formal serum-by-colistin interaction term, no conclusion can be drawn regarding statistical interaction, synergy or antagonism. Transcript abundance also cannot be assumed to reflect corresponding changes in protein abundance, respiratory activity or metabolic flux.

XH386_GM001905, annotated as an *eptA*-like phosphoethanolamine transferase, was induced not only by colistin but also during heat-inactivated serum exposure, combined serum–colistin exposure and DIP-mediated iron restriction. Phosphoethanolamine transferases can modify lipid A and contribute to polymyxin resistance [20–22], but the broad induction profile of XH386_GM001905 argues against a colistin-specific response. A second *eptA*-annotated locus showed little corresponding change, and *pmrA* was not similarly induced. These observations raise the possibility that XH386_GM001905 participates in a broader envelope-associated stress response, but functional studies would be required to determine its contribution to envelope adaptation or polymyxin susceptibility.

Several limitations should be considered. Only three strain backgrounds were examined, precluding generalization to broader antimicrobial-susceptible or carbapenem-resistant *A. baumannii* populations. The primary murine comparison used a single common inoculum, whereas the exploratory analysis incorporated the LS01 cohort from the primary experiment together with additional groups that differed in inoculum and group size; the latter was therefore interpreted descriptively. Pulmonary histopathology was assessed in separate terminal cohorts, with three mice in the common day-0 baseline group and three mice per experimental group at each subsequent time point, and no inferential between-group testing was performed. The direct three-strain growth experiment containing AB5075 represented one independent biological experiment. The non-heat-inactivated serum experiments included only two donors and did not include concentration-matched cell-free serum controls, while the heat-inactivated serum used for the biofilm and transcriptomic experiments was obtained from a single donor.
HBE-cell-associated bacterial recovery was examined in two independent experiments, but absolute recovery differed substantially between experiments and complete inoculum-normalized measurements were unavailable. The number of independent biofilm experiments also differed among conditions, and crystal-violet staining measures total attached biomass rather than viable bacterial burden. TEM observations were qualitative and were not generated using a predefined quantitative capsule-measurement framework. In addition, mobile-element and related genome annotations were derived from short-read draft assemblies and are sensitive to assembly continuity and prediction method. Finally, transcriptomic profiling was limited to XH386. The genomic and transcriptomic observations should therefore be regarded as descriptive associations rather than evidence of mechanism.

Across the experimental systems examined, acute lethality, antimicrobial resistance, surface-associated phenotypes and stress responses were not concordant among LS01, AB5075 and XH386. The differences observed between strains did not define a single pathogenicity gradient and could not be accounted for by broad functional pathway presence or absence alone.

Conclusions

LS01, AB5075 and XH386 exhibited distinct combinations of acute lethality, antimicrobial resistance, surface-associated phenotypes and responses to environmental stress. At a common murine challenge dose of 5 × 10^6 CFU, 120-h survival was 25% after LS01 infection, whereas all AB5075- and XH386-infected mice survived. In separate terminal histopathology cohorts, LS01 also showed a more sustained pulmonary injury pattern from day 2 through day 5. Greater lethality was observed in an exploratory AB5075 cohort challenged with a tenfold higher inoculum, but this observation was descriptive because the cohorts differed in inoculum and group size. XH386 yielded the highest HBE-cell-associated bacterial recovery in both independent experiments and repeatedly showed high attached biomass during exposure to 10% heat-inactivated human serum.

Major pathogenicity-, biofilm-, iron-acquisition-, secretion- and stress-associated systems were broadly shared among the three draft genomes, whereas resistance-associated gene content differed more clearly between strains. In XH386, iron restriction, heat-inactivated human serum and sub-inhibitory colistin produced distinct transcriptional responses, with the strongest induction of iron-acquisition-associated loci occurring during iron restriction. Taken together, the data show that acute lethality, surface-associated behavior and environmental stress responses can diverge substantially among *A. baumannii* strain backgrounds despite broad conservation of major functional systems.

List of abbreviations

CFU: Colony-forming unit
CRAB: Carbapenem-resistant *Acinetobacter baumannii*
DIP: 2,2′-Dipyridyl
FDR: False discovery rate
GO: Gene Ontology
HBE: Human bronchial epithelial
KEGG: Kyoto Encyclopedia of Genes and Genomes
MDR: Multidrug resistant
MIC: Minimum inhibitory concentration
MOI: Multiplicity of infection
PBS: Phosphate-buffered saline
RNA-seq: RNA sequencing
TEM: Transmission electron microscopy

Declarations

Ethics approval and consent to participate

All animal experiments were reviewed and approved by the Zhejiang University Laboratory Animal Welfare and Ethics Review Committee (approval no. ZJU20250683) and were conducted in accordance with institutional and applicable national requirements for the care and use of laboratory animals. Anesthesia, humane-endpoint monitoring, and euthanasia procedures were performed in accordance with the approved animal protocol.

De-identified residual human serum specimens obtained from individuals undergoing routine health examinations were used for the in vitro serum-exposure experiments. The use of these residual specimens was approved by the Clinical Research Ethics Committee of the First Affiliated Hospital, Zhejiang University School of Medicine (IIT Ethics Approval No. 0198; protocol no. IIT20240878B-R1). All experiments involving human-derived serum samples were conducted in accordance with the Declaration of Helsinki and relevant institutional and national guidelines and regulations. The requirement for individual informed consent was waived by the ethics committee because only de-identified residual clinical specimens were used.

Consent for publication

Not applicable.

Availability of data and materials

The previously published complete genome sequence of XH386 is available in GenBank under accession numbers CP010779.1 and CP010780.1 (BioProject PRJNA273343). The AB5075-UW reference chromosome is available in GenBank under accession number CP008706.1.

The newly generated Illumina whole-genome sequencing datasets for LS01, AB5075 and XH386, together with the RNA-sequencing datasets generated for XH386 under the five experimental conditions examined in this study, will be deposited in public sequence repositories. The corresponding BioProject, BioSample and sequence-read accession numbers will be added to the final manuscript when available.

The project-specific draft genome assemblies and associated annotation files used for direct three-strain comparative analyses and for alignment of the XH386 RNA-sequencing data will be made available together with the corresponding sequence datasets or as supplementary data, as appropriate. Phenotypic source data supporting the findings of this study will be provided in the supplementary materials.

Competing interests

YZ and HZ are named inventors on Chinese patent ZL 2026 1 0507876.8 (authorization publication no. CN 122038375 B), which relates to an alginate-based *A. baumannii* pulmonary persistence model. HY declares no competing interests.

Funding

This work was supported by the National Science and Technology Major Project Young Scientists Program (grant no. 2025ZD0549000). The funder had no role in study design, data collection, data analysis, interpretation of the results, preparation of the manuscript or the decision to submit the manuscript for publication.

Authors' contributions

YZ contributed to conceptualization, methodology, investigation, data curation, formal analysis, visualization and manuscript drafting. HY contributed to investigation and validation. HZ contributed to conceptualization, supervision, resources, funding acquisition and critical revision of the manuscript. All authors read and approved the final manuscript.

Acknowledgements

Not applicable.

References

1. World Health Organization. WHO bacterial priority pathogens list, 2024: bacterial pathogens of public health importance to guide research, development and strategies to prevent and control antimicrobial resistance. Geneva: World Health Organization; 2024.

2. Harding CM, Hennon SW, Feldman MF. Uncovering the mechanisms of *Acinetobacter baumannii* virulence. Nat Rev Microbiol. 2018;16:91–102. doi:10.1038/nrmicro.2017.148.

3. Valcek A, Philippe C, Whiteway C, Robino E, Nesporova K, Bové M, et al. Phenotypic characterization and heterogeneity among modern clinical isolates of *Acinetobacter baumannii*. Microbiol Spectr. 2023;11(1):e0306122. doi:10.1128/spectrum.03061-22.

4. Sun C, Zhou D, He J, Liu H, Fu Y, Zhou Z, et al. A panel of genotypically and phenotypically diverse clinical *Acinetobacter baumannii* strains for novel antibiotic development. Microbiol Spectr. 2024;12(8):e0008624. doi:10.1128/spectrum.00086-24.

5. King LB, Swiatlo E, Swiatlo A, McDaniel LS. Serum resistance and biofilm formation in clinical isolates of *Acinetobacter baumannii*. FEMS Immunol Med Microbiol. 2009;55:414–421. doi:10.1111/j.1574-695X.2009.00538.x.

6. Russo TA, Luke NR, Beanan JM, Olson R, Sauberan SL, MacDonald U, et al. The K1 capsular polysaccharide of *Acinetobacter baumannii* strain 307-0294 is a major virulence factor. Infect Immun. 2010;78(9):3993–4000. doi:10.1128/IAI.00366-10.

7. Geisinger E, Isberg RR. Antibiotic modulation of capsular exopolysaccharide and virulence in *Acinetobacter baumannii*. PLoS Pathog. 2015;11(2):e1004691. doi:10.1371/journal.ppat.1004691.

8. Talyansky Y, Nielsen TB, Yan J, Carlino-MacDonald U, Di Venanzio G, Chakravorty S, et al. Capsule carbohydrate structure determines virulence in *Acinetobacter baumannii*. PLoS Pathog. 2021;17(2):e1009291. doi:10.1371/journal.ppat.1009291.

9. Kamuyu G, Ercoli G, Ramos-Sevillano E, Willcocks S, Kewcharoenwong C, Kiratisin P, et al. Strain specific variations in *Acinetobacter baumannii* complement sensitivity. Front Immunol. 2022;13:853690. doi:10.3389/fimmu.2022.853690.

10. Saren C, Oinuma KI, Tsubouchi T, Sakiyama A, Suzuki M, Niki M, et al. Benefits and costs of a hypercapsule and the mechanism of its loss in a clinical isolate of *Acinetobacter baumannii*. mBio. 2026;17(2):e0236625. doi:10.1128/mbio.02366-25.

11. Gaddy JA, Tomaras AP, Actis LA. The *Acinetobacter baumannii* 19606 OmpA protein plays a role in biofilm formation on abiotic surfaces and in the interaction of this pathogen with eukaryotic cells. Infect Immun. 2009;77(8):3150–3160. doi:10.1128/IAI.00096-09.

12. Smani Y, McConnell MJ, Pachón J. Role of fibronectin in the adhesion of *Acinetobacter baumannii* to host cells. PLoS One. 2012;7(4):e33073. doi:10.1371/journal.pone.0033073.

13. Tomaras AP, Dorsey CW, Edelmann RE, Actis LA. Attachment to and biofilm formation on abiotic surfaces by *Acinetobacter baumannii*: involvement of a novel chaperone-usher pili assembly system. Microbiology (Reading). 2003;149(Pt 12):3473–3484. doi:10.1099/mic.0.26541-0.

14. Choi AHK, Slamti L, Avci FY, Pier GB, Maira-Litrán T. The *pgaABCD* locus of *Acinetobacter baumannii* encodes the production of poly-β-1,6-N-acetylglucosamine, which is critical for biofilm formation. J Bacteriol. 2009;191(19):5953–5963. doi:10.1128/JB.00647-09.

15. Ahmad I, Nadeem A, Mushtaq F, Zlatkov N, Shahzad M, Zavialov AV, et al. Csu pili dependent biofilm formation and virulence of *Acinetobacter baumannii*. NPJ Biofilms Microbiomes. 2023;9:101. doi:10.1038/s41522-023-00465-6.

16. Cook-Libin S, Sykes EME, Kornelsen V, Kumar A. Iron acquisition mechanisms and their role in the virulence of *Acinetobacter baumannii*. Infect Immun. 2022;90:e00223-22. doi:10.1128/iai.00223-22.

17. Sheldon JR, Skaar EP. *Acinetobacter baumannii* can use multiple siderophores for iron acquisition, but only acinetobactin is required for virulence. PLoS Pathog. 2020;16:e1008995. doi:10.1371/journal.ppat.1008995.

18. Penwell WF, Arivett BA, Actis LA. The *Acinetobacter baumannii* entA gene located outside the acinetobactin cluster is critical for siderophore production, iron acquisition and virulence. PLoS One. 2012;7(5):e36493. doi:10.1371/journal.pone.0036493.

19. Ten KE, Rahman S, Tan HS. Transcriptomic insights into the virulence of *Acinetobacter baumannii* during infection—role of iron uptake and siderophore production genes. FEBS Lett. 2025;599(1):120–139. doi:10.1002/1873-3468.15061.

20. Novović K, Jovčić B. Colistin resistance in *Acinetobacter baumannii*: molecular mechanisms and epidemiology. Antibiotics (Basel). 2023;12:516. doi:10.3390/antibiotics12030516.

21. Arroyo LA, Herrera CM, Fernandez L, Hankins JV, Trent MS, Hancock REW. The pmrCAB operon mediates polymyxin resistance in *Acinetobacter baumannii* ATCC 17978 and clinical

isolates through phosphoethanolamine modification of lipid A. Antimicrob Agents Chemother. 2011;55(8):3743–3751. doi:10.1128/AAC.00256-11.

22. Potron A, Vuillemenot JB, Puja H, Triponney P, Bour M, Valot B, et al. ISAba1-dependent overexpression of eptA in clinical strains of *Acinetobacter baumannii* resistant to colistin. J Antimicrob Chemother. 2019;74(9):2544–2550. doi:10.1093/jac/dkz241.

23. Sato Y, Unno Y, Ubagai T, Ono Y. Sub-minimum inhibitory concentrations of colistin and polymyxin B promote *Acinetobacter baumannii* biofilm formation. PLoS One. 2018;13(3):e0194556. doi:10.1371/journal.pone.0194556.

24. Lurie-Weinberger MN, Cohen A, Kon H, Kastel O, Keren-Paz A, Schwartz D, et al. Virulence factors are preserved within carbapenem-resistant *Acinetobacter baumannii* clades. Virulence. 2025;16(1):2542489. doi:10.1080/21505594.2025.2542489.

25. Sharma S, Singh K, Chaurasiya A, Banerjee T, Singh R, Yadav G, et al. Comparative study of phenotypic and genotypic expression of virulence factors in colonizing and pathogenic carbapenem resistant *Acinetobacter baumannii* (CRAB). BMC Microbiol. 2025;25:13. doi:10.1186/s12866-024-03727-1.

26. Zhou H, Larkin PMK, Huang J, Yao Y, Zhu B, Yang Q, et al. Discovery of a novel hypervirulent *Acinetobacter baumannii* strain in a case of community-acquired pneumonia. Infect Drug Resist. 2020;13:1147–1153. doi:10.2147/IDR.S244044.

27. Jacobs AC, Thompson MG, Black CC, Kessler JL, Clark LP, McQueary CN, et al. AB5075, a highly virulent isolate of *Acinetobacter baumannii*, as a model strain for the evaluation of pathogenesis and antimicrobial treatments. mBio. 2014;5:e01076-14. doi:10.1128/mBio.01076-14.

28. Fang Y, Quan J, Hua X, Feng Y, Li X, Wang J, et al. Complete genome sequence of *Acinetobacter baumannii* XH386 (ST208), a multidrug-resistant bacterium isolated from a pediatric hospital in China. Genom Data. 2016;7:269–274. doi:10.1016/j.gdata.2015.12.002.

29. Clinical and Laboratory Standards Institute. Performance standards for antimicrobial susceptibility testing. 36th ed. CLSI supplement M100. Wayne, PA: Clinical and Laboratory Standards Institute; 2026.

30. Alcock BP, Huynh W, Chalil R, Smith KW, Raphenya AR, Wlodarski MA, et al. CARD 2023: expanded curation, support for machine learning, and resistome prediction at the Comprehensive Antibiotic Resistance Database. Nucleic Acids Res. 2023;51(D1):D690–D699. doi:10.1093/nar/gkac920.

31. Chen S, Zhou Y, Chen Y, Gu J. fastp: an ultra-fast all-in-one FASTQ preprocessor. Bioinformatics. 2018;34(17):i884–i890. doi:10.1093/bioinformatics/bty560.

32. Langmead B, Salzberg SL. Fast gapped-read alignment with Bowtie 2. Nat Methods. 2012;9(4):357–359. doi:10.1038/nmeth.1923.

33. Liao Y, Smyth GK, Shi W. featureCounts: an efficient general purpose program for assigning sequence reads to genomic features. Bioinformatics. 2014;30(7):923–930. doi:10.1093/bioinformatics/btt656.

34. Love MI, Huber W, Anders S. Moderated estimation of fold change and dispersion for RNA-seq data with DESeq2. Genome Biol. 2014;15:550. doi:10.1186/s13059-014-0550-8.

35. Wu T, Hu E, Xu S, Chen M, Guo P, Dai Z, et al. clusterProfiler 4.0: a universal enrichment tool for interpreting omics data. Innovation (Camb). 2021;2(3):100141. doi:10.1016/j.xinn.2021.100141.

36. Peleg AY, Jara S, Monga D, Eliopoulos GM, Moellering RC Jr, Mylonakis E. *Galleria mellonella* as a model system to study *Acinetobacter baumannii* pathogenesis and therapeutics. Antimicrob Agents Chemother. 2009;53(6):2605–2609. doi:10.1128/AAC.01533-08.

37. Harris G, KuoLee R, Lam CK, Kanzaki G, Patel GB, Xu HH, et al. A mouse model of *Acinetobacter baumannii*-associated pneumonia using a clinically isolated hypervirulent strain. Antimicrob Agents Chemother. 2013;57:3601–3613. doi:10.1128/AAC.00944-13.

38. Gebhardt MJ, Gallagher LA, Jacobson RK, Usacheva EA, Peterson LR, Zurawski DV, et al. Joint transcriptional control of virulence and resistance to antibiotic and environmental stress in *Acinetobacter baumannii*. mBio. 2015;6(6):e01660-15. doi:10.1128/mBio.01660-15.

Supplementary material

Supplementary Table S1. Complete MIC profiles of LS01, AB5075 and XH386.

Supplementary Table S2. Draft-genome assembly and predicted genomic-component characteristics of LS01, AB5075 and XH386.

Supplementary Table S3. Distribution of selected pathogenicity-, biofilm-, iron-acquisition-, secretion- and stress-associated annotations among LS01, AB5075 and XH386.

Supplementary Table S4. CARD antimicrobial-resistance-associated annotations for LS01, AB5075 and XH386.

Supplementary Table S5. Complete RNA-seq differential-expression results.

Supplementary Table S6. Selected iron-acquisition and envelope-associated transcriptomic modules in XH386.

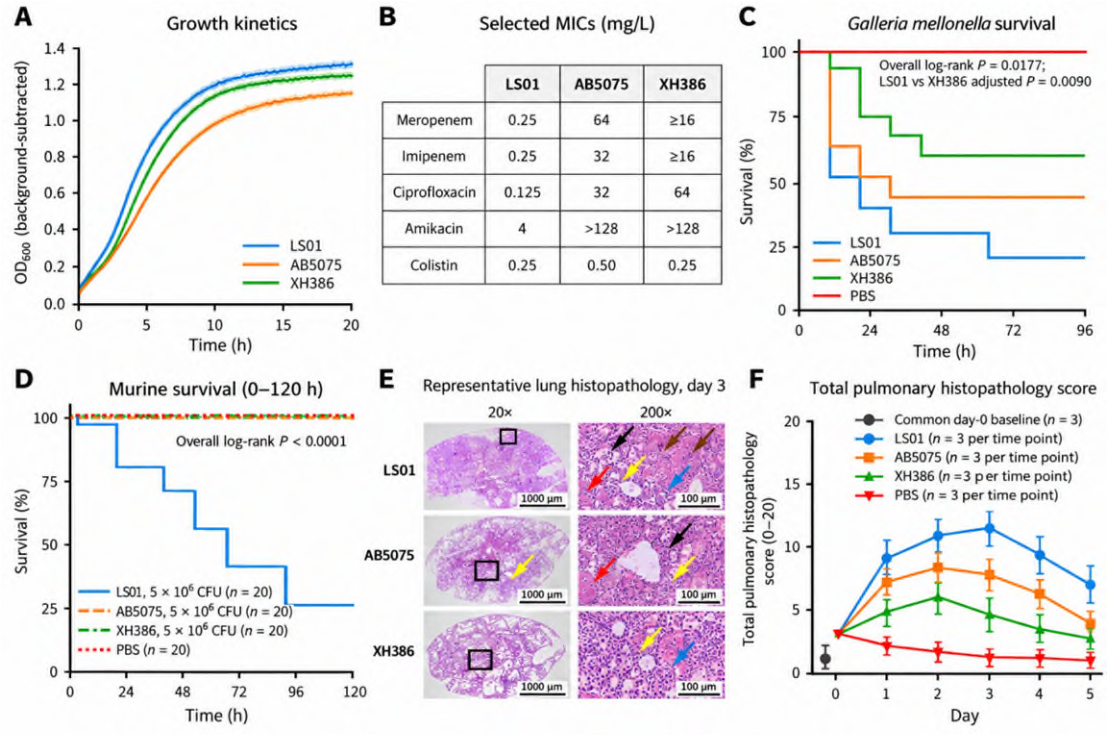
Supplementary Figure S1. Exploratory murine dose-ranging survival analysis through 120 h using the LS01 cohort from the primary experiment and additional XH386 and higher-dose AB5075 cohorts.

Supplementary Figure S2. Additional growth-curve data.

Supplementary Figure S3. Comparative GO, KEGG and selected VFDB/PHI-base annotation summaries.

Supplementary Figure S4. RNA-seq sample correlation matrix and additional differential-expression analyses.

Supplementary Data S1. Source data for growth, Galleria survival, primary and exploratory mouse survival, serum exposure, HBE-cell association, biofilm and iron-response experiments.



	LS01	AB5075	XH386
Meropenem	0.25	64	≥16
Imipenem	0.25	32	≥16
Ciprofloxacin	0.125	32	64
Amikacin	4	>128	>128
Colistin	0.25	0.50	0.25

Figure 1. Growth characteristics, antimicrobial susceptibility, acute lethality and pulmonary histopathology of LS01, AB5075 and XH386.

(A) Growth curves of LS01, AB5075 and XH386 cultured in LB broth under identical conditions. OD600 values were background-subtracted using the mean signal from three medium-only control wells. Curves represent the mean of 12 technical wells per strain from one independent biological experiment and are presented descriptively.
(B) Selected minimum inhibitory concentrations (MICs) illustrating differences in antimicrobial susceptibility among the three strains. Values are expressed in mg/L.
(C) Kaplan–Meier survival curves for *Galleria mellonella* challenged with 5 × 10^4 CFU per larva (n = 20 per bacterial group); PBS-injected larvae served as controls. Overall survival differed among the three bacterial groups (log-rank $P = 0.0177$). After Holm adjustment, the LS01-versus-XH386 comparison remained significant (adjusted $P = 0.0090$).
(D) Kaplan–Meier survival curves from the primary equal-dose murine pulmonary infection experiment. C57BL/6J mice were challenged by oropharyngeal aspiration with 5 × 10^6 CFU of LS01, AB5075 or XH386 (n = 20 per bacterial group) and followed for 120 h. Animals euthanized after reaching prespecified humane endpoints were treated as deaths at the corresponding observation time. Overall survival differed among the three bacterial groups (log-rank $P < 0.0001$).
(E) Representative H&E-stained lung sections collected on day 3 from the separate terminal histopathology cohorts. Low-magnification images are shown at 20× and corresponding high-magnification images at 200×. Scale bars, 1000 µm at 20× and 100 µm at 200×.
(F) Longitudinal total pulmonary histopathology scores from day 0 to day 5. A common uninfected baseline cohort was examined at day 0 (n = 3), and three mice per experimental group were examined at each prespecified time point from day 1 through day 5. Five pulmonary lesion domains—alveolar-wall thickening, inflammatory-cell infiltration, bronchial epithelial-cell injury/necrosis, vascular congestion and hemorrhage—were each graded independently from 0 to

4, and the five domain scores were summed to generate an animal-level total score ranging from 0 to 20. Points and error bars indicate mean ± SD. Histopathology data were interpreted descriptively, and no inferential between-group testing was performed.

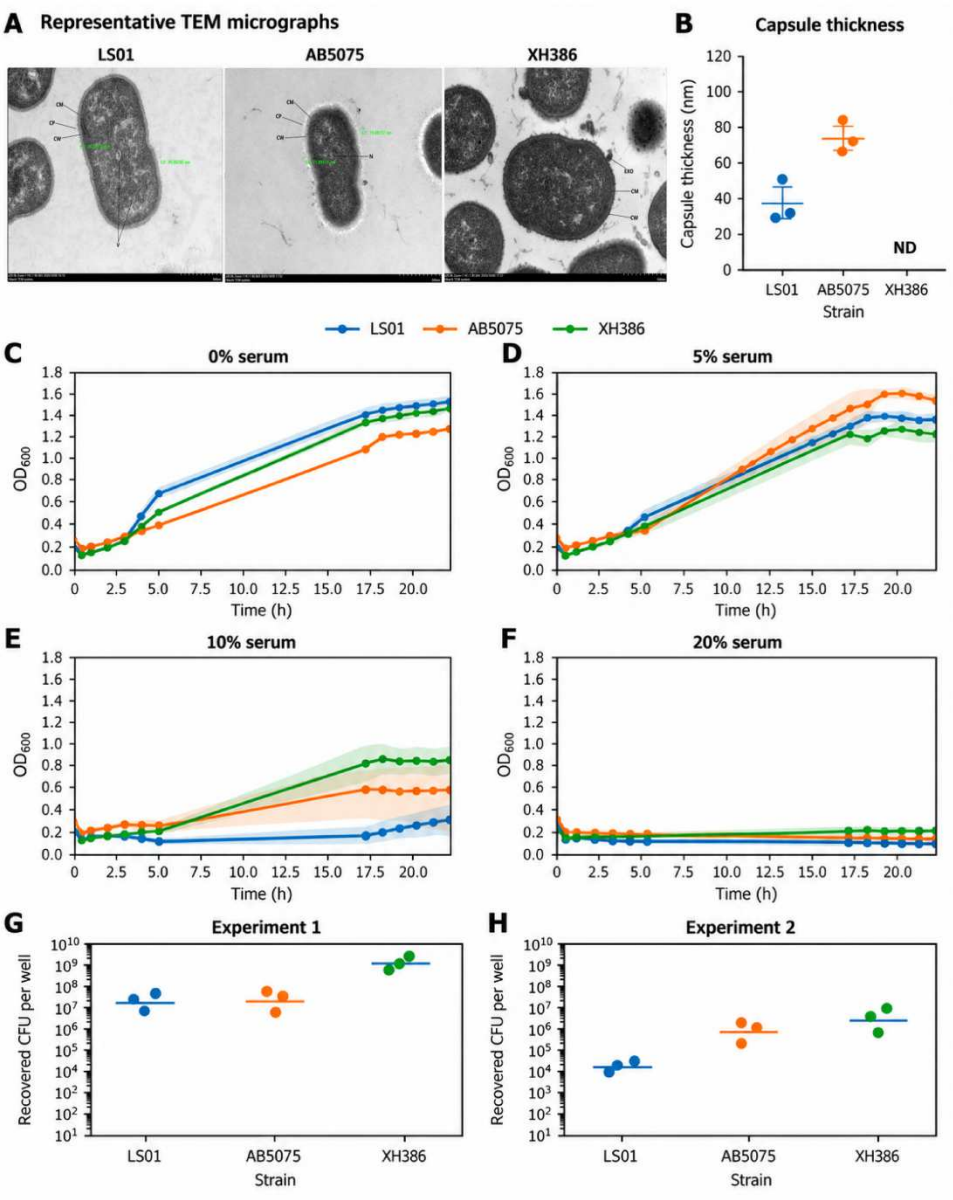


Figure 2. Surface-associated and host-related phenotypes of LS01, AB5075 and XH386.
(A) Representative transmission electron micrographs of logarithmic-phase LS01, AB5075 and XH386. AB5075 showed a prominent and relatively continuous capsule-associated extracellular layer, LS01 showed a thinner and less continuous layer, and XH386 showed markedly attenuated capsule-associated material. Green annotations indicate apparent capsule-thickness measurements in representative sections. CP, capsule-associated material; CW, cell wall; CM, cytoplasmic membrane. Scale bars, 500 nm. **(B)** Descriptive capsule-thickness measurements obtained from representative TEM sections. Individual measurements are shown for LS01 and AB5075, with summary bars indicating mean ± SD. Capsule-associated material in XH386 was largely absent and could not be reliably measured; this group is indicated as not detected (ND). These measurements were descriptive and were not subjected to inferential statistical testing. **(C–F)** OD600 trajectories of LS01, AB5075 and XH386 during exposure to 0%, 5%, 10% and 20% non-heat-inactivated human serum, respectively. Curves represent the mean of three technical

replicate wells within the displayed donor experiment, and shaded regions indicate SD. Because concentration-matched cell-free serum blanks were not included, OD600 values are presented as growth-associated optical-density measurements, and absolute comparisons across serum concentrations should be interpreted cautiously. **(G,H)** HBE-cell-associated bacterial recovery in two independent biological experiments. Three technical replicate wells were analyzed per strain in each experiment. Individual points represent technical replicate wells, and horizontal bars indicate geometric means. The y-axis is logarithmic. Results are reported as recovered HBE-cell-associated CFU per well rather than adhesion efficiency because complete inoculum-normalized measurements were not available for all experiments.

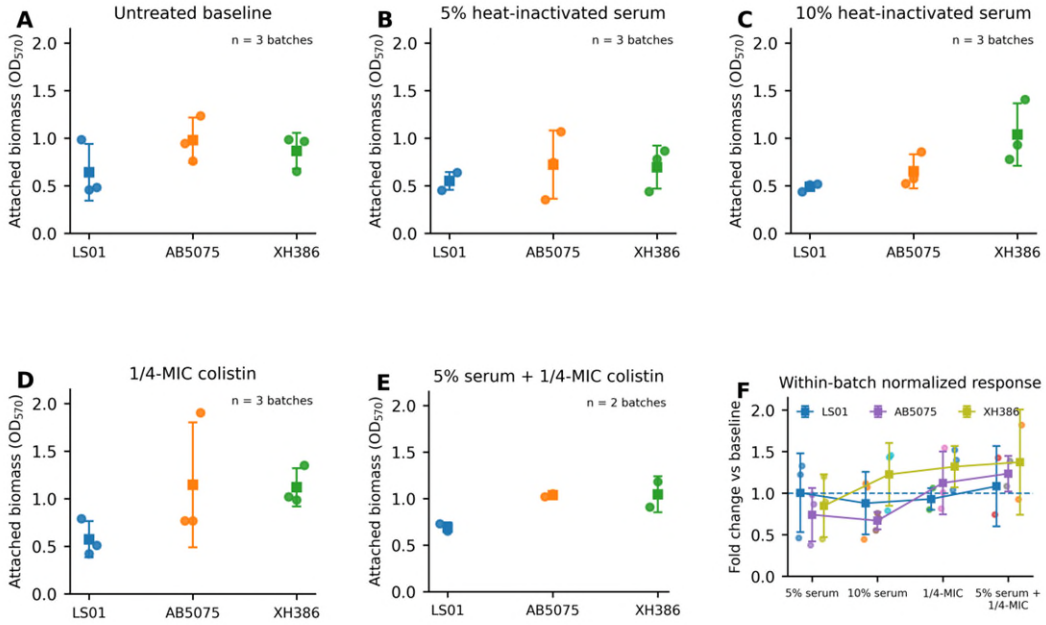


Figure 3. Strain- and condition-dependent changes in attached biofilm biomass in LS01, AB5075 and XH386.

(A) Untreated attached biomass. **(B,C)** Attached biomass during exposure to 5% and 10% heat-inactivated human serum, respectively. **(D)** Attached biomass during exposure to strain-specific 1/4-MIC colistin. **(E)** Attached biomass during combined exposure to 5% heat-inactivated serum and 1/4-MIC colistin. Individual circles represent the mean of technical replicate wells within an independent experimental batch; squares and error bars indicate mean ± SD across independent batches. Three independent batches were available for panels A–D and two for panel E. **(F)** Within-batch treatment responses normalized to the corresponding untreated baseline. Small points represent independent batch-level ratios, and squares with error bars indicate mean ± SD. Crystal-violet absorbance was measured at 570 nm and represents total attached biomass rather than viable bacterial burden. No inferential statistical testing was applied because of the limited number of independent experimental batches.

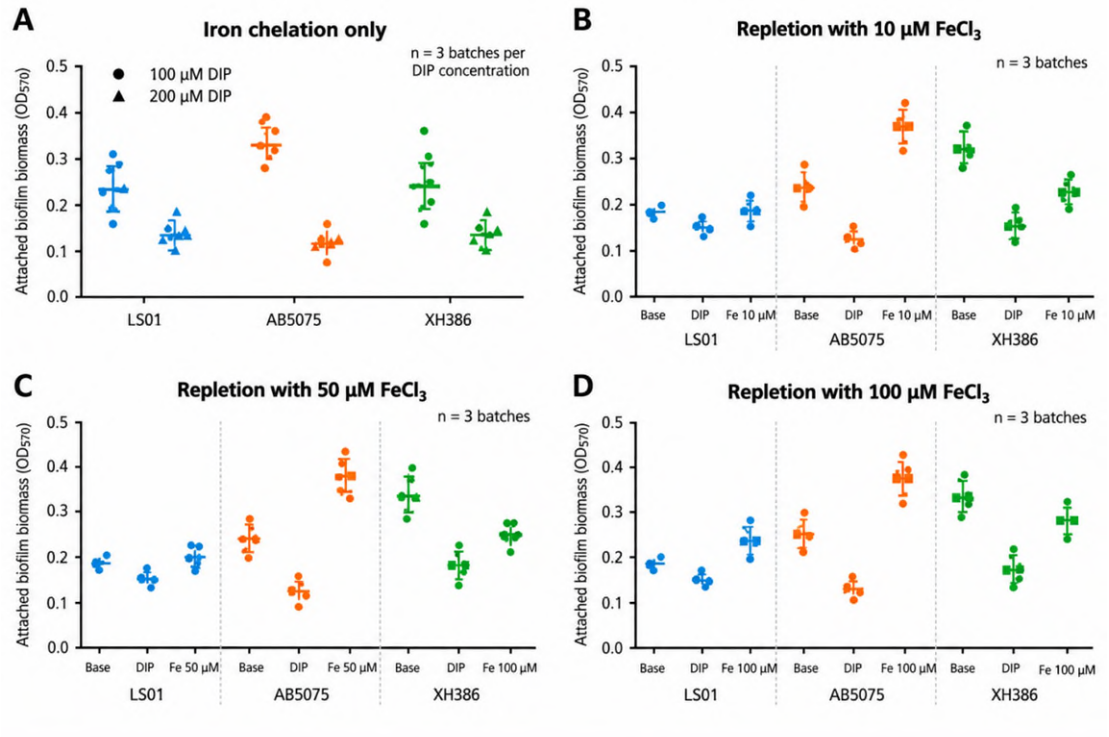
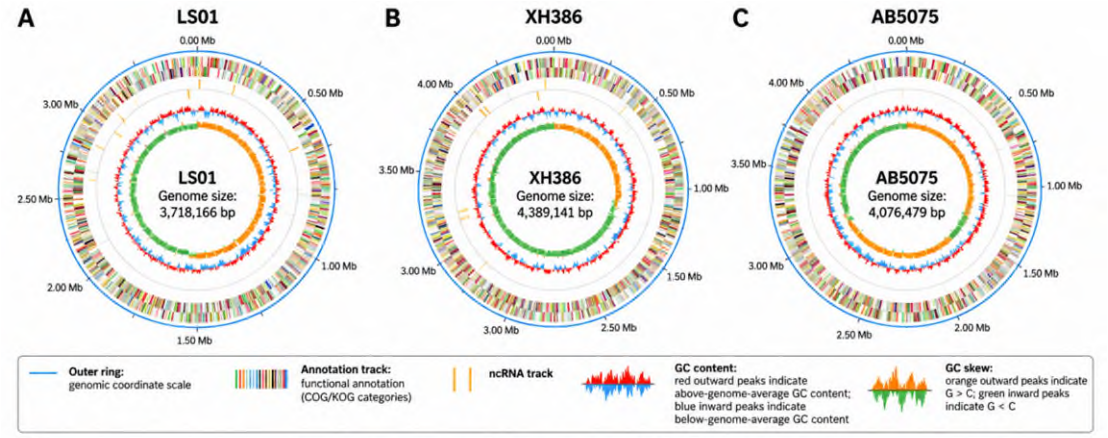


Figure 4. Strain-dependent changes in attached biofilm biomass during iron chelation and iron repletion.

(A) Attached biofilm biomass of LS01, AB5075 and XH386 during iron chelation with 100 or 200 µM 2,2′-dipyridyl (DIP). Circles indicate 100 µM DIP and triangles indicate 200 µM DIP. Individual points represent independent experimental-batch values after averaging technical replicate wells within each batch. Three independent batches were examined at each DIP concentration. Summary markers and error bars indicate mean ± SD across independent batches.

(B–D) Attached biofilm biomass following iron repletion with 10, 50 or 100 µM $FeCl_3$, respectively, against a 100 µM DIP background. For each strain, untreated baseline, DIP-only and $FeCl_3$-supplemented conditions from the same experimental batch are shown. Individual points represent independent batch-level values after averaging technical replicate wells; squares and error bars indicate mean ± SD across three independent batches.

Crystal-violet absorbance was measured at 570 nm and reflects total attached biomass rather than viable bacterial burden. Iron-repletion conditions were interpreted relative to the corresponding DIP-only condition within the same experimental batch. The data were analyzed descriptively, and no inferential between-group statistical testing was performed.



D

Comparative phenotypic and genomic features of LS01, AB5075 and XH386

Feature	LS01	AB5075	XH386
Murine survival at 5 × 10^6 CFU	25% (5/20)	100% (20/20)	100% (20/20)
G. mellonella survival at 96 h (5 × 10^4 CFU)	20% (4/20)	45% (9/20)	60% (12/20)
Antimicrobial phenotype	Broadly susceptible	MDR/CRAB	MDR/CRAB
Capsule-associated morphology (TEM)	Thinner layer	Prominent layer	Markedly attenuated layer
HBE-cell-associated recovery	Lower in both experiments	Intermediate/variable	Highest in both experiments
Attached biofilm biomass (10% serum)	Lower	Intermediate/variable	Highest in repeated experiments
Iron-restriction transcriptome	Not assessed	Not assessed	Strong transcriptional response (1,059 DEGs, adjusted $P < 0.05$, $\|\log2FC\| \geq 1$)
Uniform draft assembly size	3,718,166 bp (3.72 Mb)	4,076,479 bp (4.08 Mb)	4,389,141 bp (4.39 Mb)

Figure 5. Comparative genome architecture and phenotypic characteristics of LS01, AB5075 and XH386.

(A–C) Circular genome maps of the uniformly generated draft assemblies of LS01, XH386 and AB5075, respectively. The corresponding assembly sizes were 3,718,166 bp for LS01, 4,389,141 bp for XH386 and 4,076,479 bp for AB5075. The outer ring indicates genomic coordinates. Inner tracks show functional annotations, predicted non-coding RNA features, GC content and GC skew. For the GC-content track, outward red peaks indicate regions with GC content above the genome-wide average and inward blue peaks indicate regions below the genome-wide average. For the GC-skew track, outward orange peaks indicate G > C and inward green peaks indicate G < C. The maps are shown as descriptive representations of the three uniformly generated draft assemblies.

(D) Summary of selected phenotypic and genomic characteristics of LS01, AB5075 and XH386. At the common murine challenge dose of 5 × 10^6 CFU, 120-h survival was 25% for LS01 and 100% for both AB5075 and XH386. In *Galleria mellonella* challenged with 5 × 10^4 CFU, 96-h survival was 20%, 45% and 60% for LS01, AB5075 and XH386, respectively. LS01 was broadly antimicrobial susceptible, whereas AB5075 and XH386 showed MDR/CRAB phenotypes. Representative TEM sections showed a thinner capsule-associated layer in LS01, a prominent layer in AB5075 and markedly attenuated capsule-associated material in XH386. XH386 yielded the highest HBE-cell-associated bacterial recovery in both independent experiments and repeatedly showed the highest attached biomass during exposure to 10% heat-inactivated human serum. Transcriptomic profiling under iron restriction was performed only for XH386 and showed a strong response, with 1,059 genes meeting adjusted $P < 0.05$ and |log2 fold change| ≥ 1. The summary is intended to illustrate the differing combinations of phenotypic and genomic features across the three strains and not to define a single hierarchy of pathogenicity.

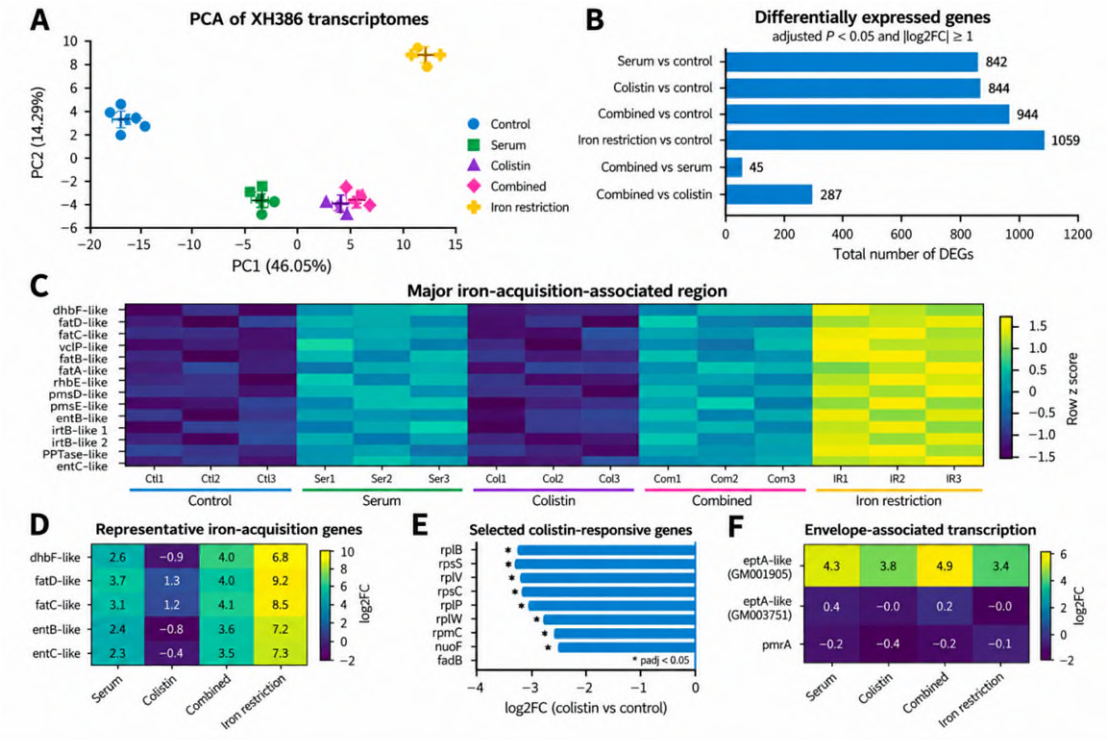


Figure 6. Environmental stresses induce distinct transcriptional states in XH386.

(A) Principal-component analysis of 15 XH386 RNA-seq samples representing five experimental conditions: untreated control, 10% heat-inactivated human serum, 1/2-MIC colistin, combined 10% heat-inactivated human serum plus 1/2-MIC colistin, and 100 μM 2,2′-dipyridyl (DIP)-mediated iron restriction. Each condition comprised three independent biological replicates. PC1 and PC2 accounted for 46.05% and 14.29% of the total variance, respectively.

(B) Total numbers of differentially expressed genes in the six prespecified pairwise contrasts. Genes were included when the adjusted *P* value was <0.05 and the absolute log2 fold change was ≥1. The numbers of genes meeting both criteria were 842 for serum versus control, 844 for colistin versus control, 944 for combined serum–colistin versus control, 1,059 for iron restriction versus control, 45 for combined serum–colistin versus serum alone, and 287 for combined serum–colistin versus colistin alone.

(C) Expression profiles of genes within a major iron-acquisition-associated region across all 15 XH386 samples. FPKM values were log2-transformed and standardized by gene as row z-scores. Columns represent individual biological replicates from the control, serum, colistin, combined serum–colistin and iron-restriction conditions.

(D) Log2 fold changes of representative iron-acquisition-associated genes during exposure to 10% heat-inactivated human serum, 1/2-MIC colistin, combined serum–colistin and DIP-mediated iron restriction, each relative to untreated control. Asterisks indicate adjusted *P* < 0.05.

(E) Log2 fold changes of selected ribosomal, respiratory and metabolic genes during sub-inhibitory colistin exposure relative to untreated control. Negative values indicate reduced transcript abundance during colistin exposure. Asterisks indicate adjusted $P < 0.05$.

(F) Condition-dependent expression of two *eptA*-annotated phosphoethanolamine-transferase loci, XH386_GM001905 and XH386_GM003751, together with *pmrA*. Values indicate log2 fold changes relative to untreated control during serum, colistin, combined serum–colistin and iron-restriction conditions. Asterisks indicate adjusted $P < 0.05$.

Supplementary Files

This is a list of supplementary files associated with this preprint. Click to download.

- SupplementaryTableS2.docx
- SupplementaryFigureS1.docx